OPEN ACCESS



Modeling the Far-infrared Polarization Spectrum of a High-mass Star-forming Cloud

Dennis Lee^{1,2}, Che-Yu Chen³, Giles Novak^{1,2}, David T. Chuss⁴, Erin G. Cox¹, Kaitlyn Karpovich⁴, Peter Ashton⁵, Marc Berthoud^{1,6}, Zhi-Yun Li⁷, and Joseph M. Michail^{1,2},

¹ Center for Interdisciplinary Exploration and Research in Astrophysics (CIERA), 1800 Sherman Avenue, Evanston, IL 60201, USA

² Department of Physics & Astronomy, Northwestern University, 2145 Sheridan Road, Evanston, IL 60208, USA

³ Lawrence Livermore National Laboratory, Livermore, CA 94550, USA

⁴ Department of Physics, Villanova University, 800 E. Lancaster Avenue, Villanova, PA 19085, USA

⁵ SOFIA Science Center, NASA Ames Research Center, Moffett Field, CA 94035, USA

⁶ Engineering + Technical Support Group, University of Chicago, Chicago, IL 60637, USA

⁷ Department of Astronomy, University of Virginia, Charlottesville, VA 22904, USA

**Received 2024 May 3; revised 2024 July 8; accepted 2024 July 10; published 2024 August 28

Abstract

The polarization spectrum, or wavelength dependence of the polarization fraction, of interstellar dust emission provides important insights into the grain alignment mechanism of interstellar dust grains. We investigate the far-infrared polarization spectrum of a realistic simulated high-mass star-forming cloud under various models of grain alignment and emission. We find that neither a homogeneous grain alignment model nor a grain alignment model that includes collisional dealignment is able to produce the falling spectrum seen in observations. On the other hand, we find that a grain alignment model with grain alignment efficiency dependent on local temperature is capable of producing a falling spectrum that is in qualitative agreement with observations of OMC-1. For the model most in agreement with OMC-1, we find no correlation between the temperature and the slope of the polarization spectrum. However, we do find a positive correlation between the column density and the slope of the polarization spectrum. We suggest this latter correlation to be the result of wavelength-dependent polarization by absorption.

Unified Astronomy Thesaurus concepts: Polarimetry (1278); Interstellar dust (836); Molecular clouds (1072); Magnetohydrodynamical simulations (1966); Interstellar magnetic fields (845)

1. Introduction

While observational studies of magnetic fields in molecular clouds are difficult, they are crucial for addressing the many open questions on their role in star formation (Crutcher 2012; Li et al. 2014; Pattle & Fissel 2019). The most accessible way to carry these out is to observe the polarized emission from molecular clouds at far-infrared to millimeter wavelengths (Hildebrand et al. 2000). These measurements trace the thermal emission from magnetically aligned dust grains in the molecular clouds. Radiative alignment torques (RATs) are the leading theory for magnetic grain alignment (Dolginov & Mitrofanov 1976; Draine & Weingartner 1997; Lazarian & Hoang 2007; Andersson et al. 2015). In RAT theory, anisotropic optical/near-infrared radiation fields align irregularly shaped dust grains via the transfer of angular momentum from the radiation field to the dust grains. The end result of this process is that the grains spin about their axis of greatest moment of inertia, which are preferentially aligned with the external magnetic field. The resulting polarized emission is oriented perpendicular to the plane-of-sky projection of the magnetic field.

Using this polarized emission, numerous statistical methods have been developed to infer physical properties from observations of the magnetic field in these star-forming regions. Techniques to estimate field strength and other properties, for example, include the Davis–Chandrasekhar–Fermi (DCF) method (Davis 1951; Chandrasekhar & Fermi 1953; also see, e.g., Ostriker et al. 2001; Hildebrand et al. 2009; Chen et al. 2022; Li et al. 2022), DCF-

Original content from this work may be used under the terms of the Creative Commons Attribution 4.0 licence. Any further distribution of this work must maintain attribution to the author(s) and the title of the work, journal citation and DOI.

related polarization dispersion analysis (e.g., Houde et al. 2009, 2016; Chuss et al. 2019), and histograms of relative orientations (e.g., Soler et al. 2013; Chen et al. 2016; Planck Collaboration et al. 2016; Soler 2019; Lee et al. 2021). As a result, understanding the physics of the grain alignment mechanism is essential to ensure the proper interpretation of polarization-measurement-polarization-measurement-derived analyses (Andersson et al. 2015).

One avenue for investigating grain alignment is to study the wavelength dependence of the polarization fraction in a molecular cloud (Hildebrand et al. 1999). This polarization spectrum is created by observing the polarization fraction for a sight line as a function of the wavelength (p versus λ). The extent to which the properties of the polarization spectrum (e.g., its slope) depend on environmental conditions can potentially place constraints on the nature of the grain alignment physics (Ashton et al. 2018; Michail et al. 2021).

In molecular clouds, the far-infrared (~ 50 to $\sim 300 \,\mu\text{m}$) polarization spectrum has been observed to be falling (lower polarization fraction at longer wavelengths; Hildebrand et al. 1999; Vaillancourt et al. 2008; Zeng et al. 2013; Michail et al. 2021). Hildebrand et al. (1999) attributed this behavior to a specific effect arising in heterogeneous clouds. Michail et al. (2021) refer to this as the heterogeneous cloud effect (HCE). The HCE describes the scenario where regions with warmer grains and regions with colder grains are both present along a sight line. Grains in the warmer regions have a relatively higher grain alignment efficiency and thus emit with a higher polarization fraction. Meanwhile, grains in cooler regions have a lower grain alignment efficiency and emit with a correspondingly lower polarization fraction. As the warmer grains contribute a larger fraction of intensity at shorter wavelengths and the colder, poorly aligned grains contribute more radiation at longer wavelengths, the polarization fraction is observed to fall with wavelength. This results in the negatively sloped p versus λ behavior that has been observed (Hildebrand et al. 1999; Vaillancourt et al. 2008; Zeng et al. 2013; Michail et al. 2021).

The temperature-dependent grain alignment efficiency can be naturally explained by RATs. Grains in the warmer regions are exposed to a more intense anisotropic radiation field and hence are also expected to be better aligned. On the other hand, the grains of colder, denser regions are shielded from the radiation and are, as a result, less efficiently aligned.

Nonetheless, the falling polarization spectrum need not be explained by RATs or indeed HCE at all. In principle, it is possible that variations in the magnetic field direction within beam volume alone (so-called "field tangling") can reduce the observed polarization fraction and hence be the source of the falling spectrum. Even assuming a homogeneous grain alignment model, one expects a falling spectrum if the colder regions along a sight line suffer from more field tangling and cancellation than the warmer regions. The gravitational collapse induced by nearby star formation is one possible scenario for increased field tangling and cancellation in denser and colder regions.

Even if the HCE does operate in molecular clouds, it is possible that the alignment mechanism is actually regulated by volume density rather than directly by temperature (e.g., Ysard et al. 2013). More collisions in denser environments, for example, can "unalign" grains, resulting in lower observed polarization fractions (Andersson et al. 2015).

OMC-1, located at a distance of 390 pc as part of the Orion Nebula complex, is one of the nearest sites of massive star formation (Kounkel et al. 2017). Using the HAWC+ instrument on the Stratospheric Observatory for Infrared Astronomy (SOFIA; Harper et al. 2018), Michail et al. (2021) studied the far-infrared polarization spectrum of OMC-1. Finding an overall falling polarization spectrum, Michail et al. (2021) attributed this to the HCE. The authors argued that this result, taken together with correlations seen between the slope of the polarization spectrum and local environmental conditions, provides evidence for RATs operating in OMC-1.

In this work, we aim to test these conclusions via synthetic observations of a realistic, heterogeneous cloud simulation using various grain alignment models. We compute the polarization spectra resulting from these various grain alignment models and compare them to the OMC-1 observations. The paper is organized as follows: Section 2 reviews the polarization spectrum observations of OMC-1 with SOFIA/HAWC+ and introduces our simulation and synthetic observations. In particular, we discuss the grain alignment models we consider in Section 2.3. Section 3 presents the polarization spectrum analysis of our synthetic simulations and compares the results with the analogous analysis of the OMC-1 observations. Section 4 discusses the implications of the analysis. We present concluding thoughts in Section 5.

2. Methods

2.1. Polarimetric Observations of OMC-1

The OMC-1 region was observed using SOFIA/HAWC+ in four bands centered at 53, 89, 154, and 214 μ m with resolutions of 5", 8", 14", and 19", respectively. The polarimetric observations were conducted between 2016 December and

2018 December. Detailed descriptions of the observations and data reduction are presented in Chuss et al. (2019).

Michail et al. (2021) studied the polarization properties of OMC-1 across all four bands using these observations but adopted slightly lower resolutions (20".5 at 214 μ m) to account for additional smoothing during data reduction. In order to compare across all four bands, Michail et al. (2021) smoothed all data to 20."5 to match the lowest resolution data. In addition to typical cuts based on signal-to-noise thresholds (described in detail in Chuss et al. 2019), Michail et al. (2021) also exclude regions where the variation in polarization angles between wavelengths is greater than 15°. We discuss the impact of this in Section 2.4.

2.2. Numerical Simulation

We considered a radiation—magnetohydrodynamic (RMHD) simulation that follows the formation of massive stars in a magnetized, turbulent cloud using the ORION2 code (Li et al. 2021). The simulation was initialized as a dense cloud core of mass $M_{\rm core}=10^3\,M_\odot$ with a power-law density profile $\rho(r)\propto r^{-3/2}$ out to the radius of the core $R_{\rm core}=0.41\,{\rm pc}$. The mean column density is therefore $\Sigma\approx0.4\,{\rm g\,cm^{-2}}$ ($N_{\rm H_2}\approx10^{23}\,{\rm cm^{-2}}$), consistent with the typical range of Σ values (0.1–1 g cm⁻²) in infrared dark clouds where high-mass star formation occurs (see, e.g., the review by Motte et al. 2018). A turbulent velocity field was added to the core with Mach number $\mathcal{M}=2.43$, which corresponds to a virial parameter $\alpha_{\rm vir}=3.73$. The initially uniform magnetic field strength is chosen so that the normalized mass-to-flux ratio is 3.0 inside the core ($r < R_{\rm core}$). Three levels of adaptive mesh refinement (AMR) were applied so that the highest resolution is $\Delta x\approx 164\,{\rm au}$. For details on the treatment and application of ideal MHD with AMR in ORION2, see Li et al. (2012, 2015).

The initial gas temperature inside the core is $T_{\rm gas} = 35~{\rm K}$. This value is also set to be the temperature floor of the simulation in order to avoid tiny and/or negative temperatures from numerical rarefaction. During the formation and evolution of the protostar, radiation transport is handled by a frequency-integrated flux-limited diffusion approximation with dust opacity models from Semenov et al. (2003). More details about the protostellar model and optical properties adopted in ORION2 can be found in Offner et al. (2009) and Cunningham et al. (2011). Note that our simulation setup is almost identical to that described in Cunningham et al. (2011), but with the addition of the magnetic field to include more complete physics.

For our synthetic observation, we consider a temporal snapshot when roughly 3.5% of the cloud core mass is inside the forming protostars (two massive protostars with \sim 21 and \sim 14 M_{\odot}). At this evolutionary stage, the gas material is not overly centered around the protostars, providing a physical environment comparable to OMC-1 (see Section 2.4). A sample synthetic polarization map of our simulation is shown in Figure 1 (right panel).

2.3. Grain Alignment and Polarization Prescriptions

We use the approach described in Lam et al. (2021) and Yang (2021) to numerically calculate the polarized emission from simulations. This method—in contrast to fully solving the complicated radiative transfer process (e.g., POLARIS; Reissl et al. 2016)—allows us to test various parameters one at a time

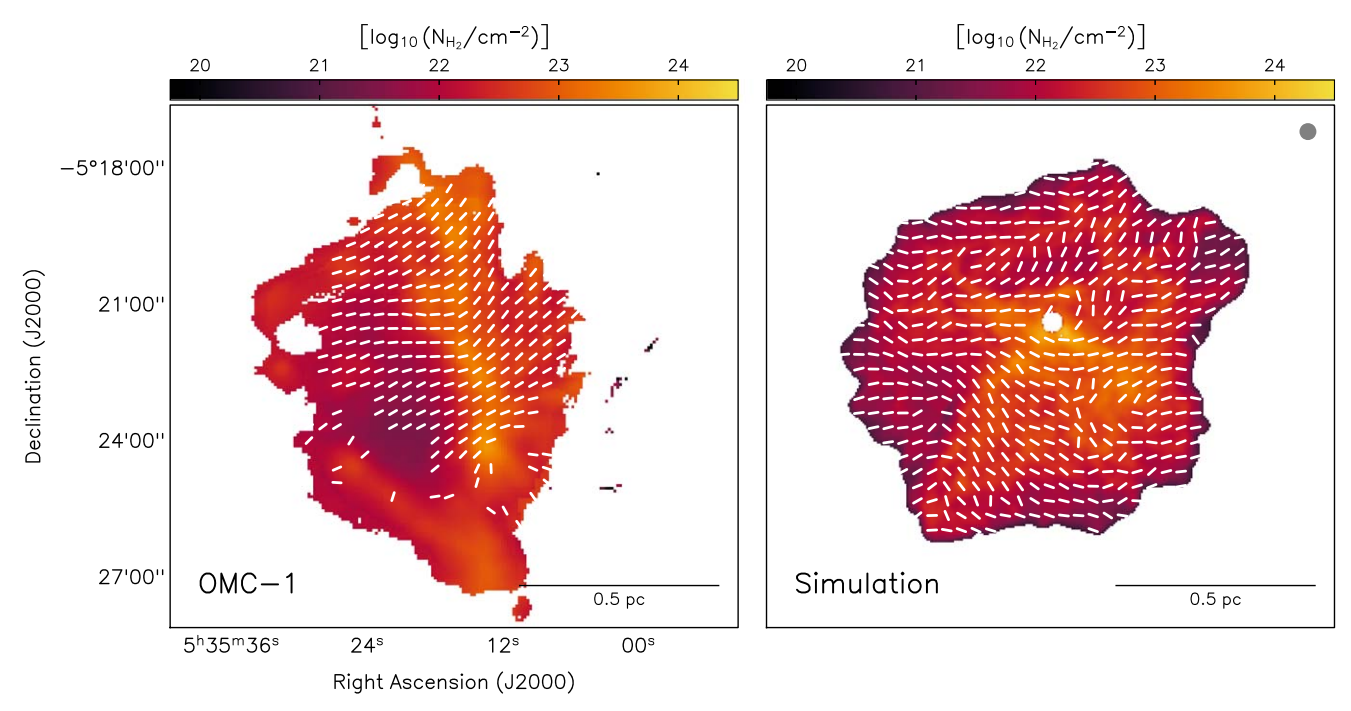


Figure 1. Maps of the column density in molecular hydrogen (N_{H2}) for OMC-1 (left) and our fiducial simulation, xi-10 (right). The column density values for OMC-1 are as computed by Chuss et al. (2019) and used in Michail et al. (2021). The column density values for our simulations were obtained via the SED fitting detailed in Section 2.4. Line segments shown in white represent the magnetic field direction inferred from the 214 μ m polarized emission. All simulation data are convolved to 20.75 in order to match the resolution of the OMC-1 observations (indicated by the beam in the upper right). Line segments are plotted every 20.75. Our simulated cloud is similar in physical extent to OMC-1, as indicated by the scale bar at the lower right of each panel. Only the xi-10 model is shown here, but all the SED-derived column density and temperature maps from the various models are similar.

to investigate the critical factors in the process of polarized emission. While the full details of this approach can be found in Lam et al. (2021) and Yang (2021), we briefly describe it here.

The fundamental criterion for magnetic alignment of spinning dust grains is that the grains have to gyrate quickly around the magnetic field before the dust–gas collisions disrupt this process. Consider the ratio between the Larmor precession timescale $t_{\rm L}$ and the gas damping timescale $t_{\rm d}$ and assume that the dust grains and gas particles are in thermal equilibrium ($T_{\rm dust} = T_{\rm gas} = T$). In this case, the magnetic alignment criterion is simply

$$\frac{t_{\rm L}}{t_{\rm d}} = 0.77 \times \left(\frac{a_{\rm mm}}{\hat{\chi}}\right) \left(\frac{B}{100 \,\mu{\rm G}}\right)^{-1} \times \left(\frac{n_{\rm g}}{10^5 \,{\rm cm}^{-3}}\right) \left(\frac{T}{15 \,{\rm K}}\right)^{3/2} < \frac{1}{n}, \tag{1}$$

or

$$\xi \equiv \frac{\hat{\chi}/\eta}{a_{\text{mm}}}$$

$$> 0.77 \times \left(\frac{B}{100 \,\mu\text{G}}\right)^{-1} \left(\frac{n_{\text{g}}}{10^5 \,\text{cm}^{-3}}\right) \left(\frac{T}{15 \,\text{K}}\right)^{3/2}, \quad (2)$$

where $a_{\rm mm}$ is the radius of individual grains in units of millimeter, $\hat{\chi}$ a dimensionless magnetic susceptibility determined by the composition of dust grains (see Yang 2021 for more details), B the magnetic field strength, $n_{\rm g}$ the number density of the gas, and η (>1) the number of gyrations per gas damping time needed for grain alignment. The value of ξ thus serves as an alignment parameter that can be used to switch

between various grain alignment prescriptions⁸ (see, e.g., Lam et al. 2021).

The polarized emission can then be derived following the method described in Lam et al. (2021) by solving the vector radiation transfer equation for the Stokes vector S = (I, Q, U):

$$\frac{1}{\rho} \frac{d}{ds} \mathbf{S} = -\mathcal{K} \, \mathbf{S} + B_{\nu}(T) \boldsymbol{a},\tag{3}$$

where ρ is the gas density, s the distance along the sight line, and $B_{\nu}(T)$ the Planck function. The extinction matrix \mathcal{K} and emission vector \boldsymbol{a} are related to the extinction and absorption opacities, which are dependent on the magnetic field structure, the alignment criterion (Equation (2)), the dust opacity κ_{ν} , and the polarizability parameter α_p (related to the maximum degree of polarization p_0 as $p_0 \approx \alpha_p/(1-\alpha_p/6)$). See Appendix B of Lam et al. (2021) for full discussions.

The formal solution of Equation (3) is

$$S = \int T(s)a B_{\nu}(T)\rho ds, \qquad (4)$$

where the matrix T(s) is obtained from the integral

$$T(s) = \prod_{s}^{\infty} e^{-\rho(s')\mathcal{K}(s')ds'}.$$
 (5)

Note that Π denotes the order-preserved geometric integration, because the extinction matrix may not be commutative. We refer the reader to Appendix B of Lam et al. (2021) for the complete calculation of S, we would like to point out that in the simplest case of optically thin dust with homogeneous

 $[\]overline{^8}$ We note that there is degeneracy in the value of ξ between $\hat{\chi}$ and $a_{\rm mm}$. While the exact value of η is uncertain, Yang (2021) suggested a fiducial value of $\eta \sim 10$.

 $(\xi \to \infty$, constant α_p) grain alignment, Equation (4) reduces to the commonly adopted equations for the Stokes parameters (Fiege & Pudritz 2000):

$$I = \int \rho \left(1 - \alpha_p \left(\frac{\cos^2 \gamma}{2} - \frac{1}{3} \right) \right) ds, \tag{6a}$$

$$Q = \alpha_p \int \rho \cos 2\psi \cos^2 \gamma \, ds, \tag{6b}$$

$$U = \alpha_p \int \rho \sin 2\psi \cos^2 \gamma \, ds, \tag{6c}$$

where ψ is the angle between the magnetic field and the direction of positive Q in the sky plane and γ is the inclination angle of the magnetic field relative to the plane of the sky.

We consider three classes of models that differ by the grain alignment properties as constrained by the grain alignment parameters, ξ and α_p :

- 1. Homogeneous: As our simplest model, we consider the scenario of perfect grain alignment. With $\xi = \infty$ and constant $\alpha_p = 0.1$ (a typical polarization level at cloud scales; see, e.g., Pattle & Fissel 2019; Pattle et al. 2023), grains throughout the simulated cloud, regardless of local conditions, are considered magnetically aligned and emit with 10% polarization fraction. The derived polarization thus depends only on the magnetic field structure as well as the optical depth effects.
- 2. Collisional depolarization: These models are based on Lam et al. (2021) for selected values of ξ (see Equation (2) for the definition). By varying ξ , thus adjusting the criterion for alignment, these models simulate the depolarization effect due to collisions between dust grains and gas particles. A lower value of ξ corresponds to a stricter grain alignment criterion. For each voxel in the simulation, grains are considered magnetically aligned if the criterion in Equation (2) is satisfied (i.e., Equation (10) of Lam et al. 2021). In addition, effects from the homogeneous model, which are related to magnetic field geometry and optical depth, remain present. We consider three values for ξ : 1, 10, and 100 (xi-1, xi-10, xi-100). We adopt ξ = 10 (xi-10) as our fiducial model.
- 3. Temperature-dependent polarizability: We extend the collisional depolarization model by adopting a power-law temperature dependence in the polarizability parameter, $\alpha_p \equiv 0.1 (T/35 \text{ K})^\zeta$ (with a maximum value set such that $\alpha_p \leqslant 0.9$). This setting allows warmer regions to have a higher degree of magnetic alignment. This is intended to model the effect of RATs whereby warmer, and hence faster-spinning grains, are better aligned with the magnetic field. We consider two different values for the power-law index ζ : 0.5 and 2.0. zeta-0.5($\alpha_p \propto T^{0.5}$) models a weaker dependence on the temperature while zeta-2 ($\alpha_p \propto T^2$) models a stronger dependence on the temperature.

2.4. Synthetic Observations

For each grain alignment prescription, we generate synthetic observations of the simulated cloud at each HAWC+ band: 53, 89, 154, and 214 μ m. Each set of synthetic observations is smoothed to the common resolution of 20.15 to match the observations (\approx 0.04 pc at d=400 pc). We select our fiducial viewing angle as 45° from both x- and z-axes such that the background magnetic field (initially along the z-axis) is oriented neither along the line of sight nor on the plane of the sky (see, e.g., Chen et al. 2019 for more discussions on viewing angle and polarization observations).

We compute the polarization fraction (p) and polarization angle (φ) from the Stokes parameters as

$$p = \frac{\sqrt{Q^2 + U^2}}{I},\tag{7}$$

$$\varphi = \frac{1}{2}\arctan\left(\frac{U}{Q}\right). \tag{8}$$

We mask regions of extremely low polarization that are not robustly detectable by observations (p < 0.002). This accounts for a small fraction of our simulation data (<0.1%).

The synthetic observations (I_{ν}) for each wavelength (λ) are then fit to a modified blackbody function for each sight line to obtain the column density (N_{H_2}) and temperature (T):

$$I_{\nu}(\lambda) = (1 - e^{-\tau_{\lambda}})B_{\nu}(T), \tag{9}$$

where the optical depth τ_{λ} is

$$\tau_{\lambda} = N_{\rm H_2} \kappa_{\lambda} \mu_{\rm H_2} m_{\rm H}. \tag{10}$$

We use $\mu_{\rm H_2}=2.8$ and $m_{\rm H}=1.6737\times 10^{-24}\,{\rm g}$. For κ_{λ} , we calculate interpolated values of the wavelength-dependent $K_{\rm abs}$ from Weingartner & Draine (2001) and Li & Draine (2001)—the same model used to generate the synthetic observations—which are then modified by a gas-to-dust ratio of 100 (i.e., $\kappa_{\lambda}=K_{\rm abs}\times 0.01\,{\rm cm^2\,g^{-1}}$).

The resulting column density and temperature values are then used for the rest of this analysis. We mask diffuse regions $(N_{\rm H_2} < 5 \times 10^{20} \, {\rm cm}^{-2})$ that are typically on the periphery of the cloud. We also mask regions that are not well fit by the modified blackbody function (e.g., sight lines that do not converge). These are largely centered on the emission peak in the center of the map (see Figure 1). Together, this accounts for approximately ~6% of the data. We also verify that the column density values obtained through the spectral energy distribution (SED) fitting procedure (median $N_{\rm H_2} = 10^{22.2} \, {\rm cm}^{-2}$) are consistent with the values computed from directly integrating the simulations along each sight line (median $N_{\rm H_2} = 10^{22.3} \, {\rm cm}^{-2}$).

Unlike Michail et al. (2021), we do not remove sight lines where the variation in polarization angles between each band is greater than 15°. This cut was done in Michail et al. (2021) in order to focus the analysis on the polarization spectrum behavior due to dust grain properties rather than field geometry. In this work, we include sight lines with variations in polarization angles so that we can consider the possibility of field geometry as contributing to the behavior of the polarization spectrum.

While our simulation setup was originally designed to study high-mass star formation processes and thus was not aimed at representing any specific star-forming cloud in particular, overall, we find that our simulated cloud is a reasonable analog

⁹ In principle, this threshold can result in a nonphysical polarization fraction of p>1 when $\alpha_p=0.9$. However, this requires T>320 K, which occurs in an insignificant number of pixels (0.009%).

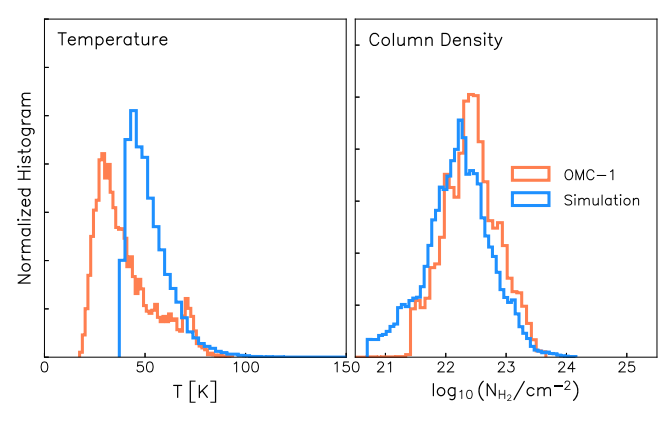


Figure 2. Temperature distribution (left) and column density distribution (right) of OMC-1 (orange) and our synthetic observations (blue), respectively. Temperature and column density values for the synthetic simulations were obtained via the SED fitting detailed in Section 2.4. While our simulated cloud is overall warmer than OMC-1, both our simulated cloud and OMC-1 show similar column density distributions.

for OMC-1. As shown in Figure 1, the simulated cloud has a similar physical size as OMC-1 (assuming a distance of \sim 390 pc). The inferred magnetic field direction derived from the 214 μ m observations of OMC-1 and the simulations are overlaid in Figure 1. The circular standard deviation of the inferred field direction for the observations and the simulations are not too different at 21° and 35°, respectively. Figure 2 shows the column density and temperature distributions of OMC-1 compared to our simulation. Both our simulated cloud and OMC-1 show similar column density distributions with a median of $\log_{10}(N_{\rm H_2}/{\rm cm}^{-2}) \approx 22$ (22.2 and 22.4 for the simulation and OMC-1, respectively). The temperature distribution of our simulated cloud is somewhat higher ($\sim 1.4 \times$). This is likely, at least in part, due to the 35 K initial gas temperature and temperature floor of our simulation (see Section 2.2). Finally, Michail et al. (2021) report that about 25% of their sight lines have $\tau_{53} \ge 0.5$. For our synthetic sight lines, we report 28% of sight lines with $\tau_{53} \ge 0.5$ in OMC-1. In summary, despite some modest differences, our simulation provides a suitable proxy for studying the physics of OMC-1.

3. Analysis and Results

3.1. Global Polarization Spectrum

For each set of synthetic observations, we produce the global polarization spectrum by finding the median value of the polarization fraction ratio (p_{λ}/p_{214}) across the cloud. The associated median absolute deviation (MAD) values are also calculated. These are shown in Figure 3 and Table 1, which also include the analogous results obtained for OMC-1 by Michail et al. (2021).

The homogeneous grain alignment model (homogeneous) produces a relatively flat global polarization spectrum (Figure 3(a)) indicating consistent polarization fractions across the four bands.

The global polarization spectrum of models using the collisional depolarization grain alignment model (xi-1, xi-10, xi-100) shows a flat or increasing polarization spectrum (Figure 3(b)). Varying the alignment parameter ξ in our grain alignment model changes the spectrum shape from rising at low values of ξ to a flatter shape at high values of ξ (Figure 3(b)). As expected, at large ξ values, the grain alignment model approaches the model of uniform grain

Table 1Global Polarization Spectrum

Model	p_{53}/p_{214}	p_{89}/p_{214}	p_{154}/p_{214}
Homogeneous	0.97 ± 0.13	0.99 ± 0.05	1.00 ± 0.01
xi-10	0.94 ± 0.15	0.97 ± 0.05	0.99 ± 0.01
zeta-0.5	1.04 ± 0.25	1.01 ± 0.08	1.00 ± 0.02
zeta-2	1.29 ± 0.33	1.09 ± 0.10	1.02 ± 0.02
OMC-1 ^a	1.19 ± 0.32	1.19 ± 0.21	0.99 ± 0.09

Notes. The median polarization fraction at each HAWC+ band (53 μ m, 89 μ m, 154 μ m) normalized to the longest HAWC+ band at 214 μ m.

alignment ($\xi = \infty$). None of these collisional depolarization grain alignment models (Figure 3(b))—regardless of ξ —produced a falling polarization spectrum.

Figure 3(c) shows the fiducial collisional depolarization model (xi-10) in the nominal viewing angle along with two different viewing angles. The Z-view model represents the viewing angle along the initial direction of the magnetic field. The X-view model represents a viewing angle where the magnetic field is orthogonal to the line of sight. Despite the different projected magnetic field directions when viewed from different angles, analysis of the synthetic observations along all three viewing angles results in a rising polarization spectrum (i.e., positive slope). This suggests that the projected magnetic field morphology is not the key parameter contributing to the wavelength-dependent polarization fraction.

Extending our investigations to test the concept of RATs, we considered two models where α_p is dependent on the temperature (temperature-dependent polarizability models; zeta-0.5, zeta-2). By adding a simple power-law dependence on the temperature to the polarization coefficient $\alpha_p(T) \equiv 0.1(T/35 \text{ K})^{\zeta}$ (see Section 2.3), our fiducial model (xi-10) changed from a rising polarization spectrum to a falling spectrum. The results are shown in Figure 3(d), which also indicates that the model with the strongest dependence on the temperature (zeta-2) has a more steeply falling overall spectrum comparable to the polarization spectrum observed in OMC-1. We discuss the possible origins of the falling polarization spectrum in detail in Section 4.1.

3.2. Pixel-by-pixel Polarization Spectrum

To investigate any effect local environments can have on the polarization spectrum, we look for quantitative variations in the polarization spectra computed individually for each pixel of our multiwavelength synthetic polarization maps. We fit these pixel-by-pixel polarization spectra to the form (Gandilo et al. 2016; Shariff et al. 2019; Michail et al. 2021):

$$p(\lambda)/p(\lambda_0) = a_{\ell}[b_{\ell}(\lambda - \lambda_0) + 1]. \tag{11}$$

As before, we use $214 \,\mu\mathrm{m}$ as the normalizing wavelength (i.e., $\lambda_0 = 214 \,\mu\mathrm{m}$). The shape of the polarization spectrum is thus characterized by the b_ℓ parameter. ¹⁰ A positive value for b_ℓ indicates a rising spectrum (i.e., polarization increasing with wavelength). A negative value for b_ℓ indicates a falling

^a OMC-1 results from Michail et al. (2021).

¹⁰ The "true" slope is given by $a_{\ell} \times b_{\ell}$, but as $a_{\ell} \approx 1$ in our results (see Table 2), we use b_{ℓ} as a proxy for the slope throughout this work.

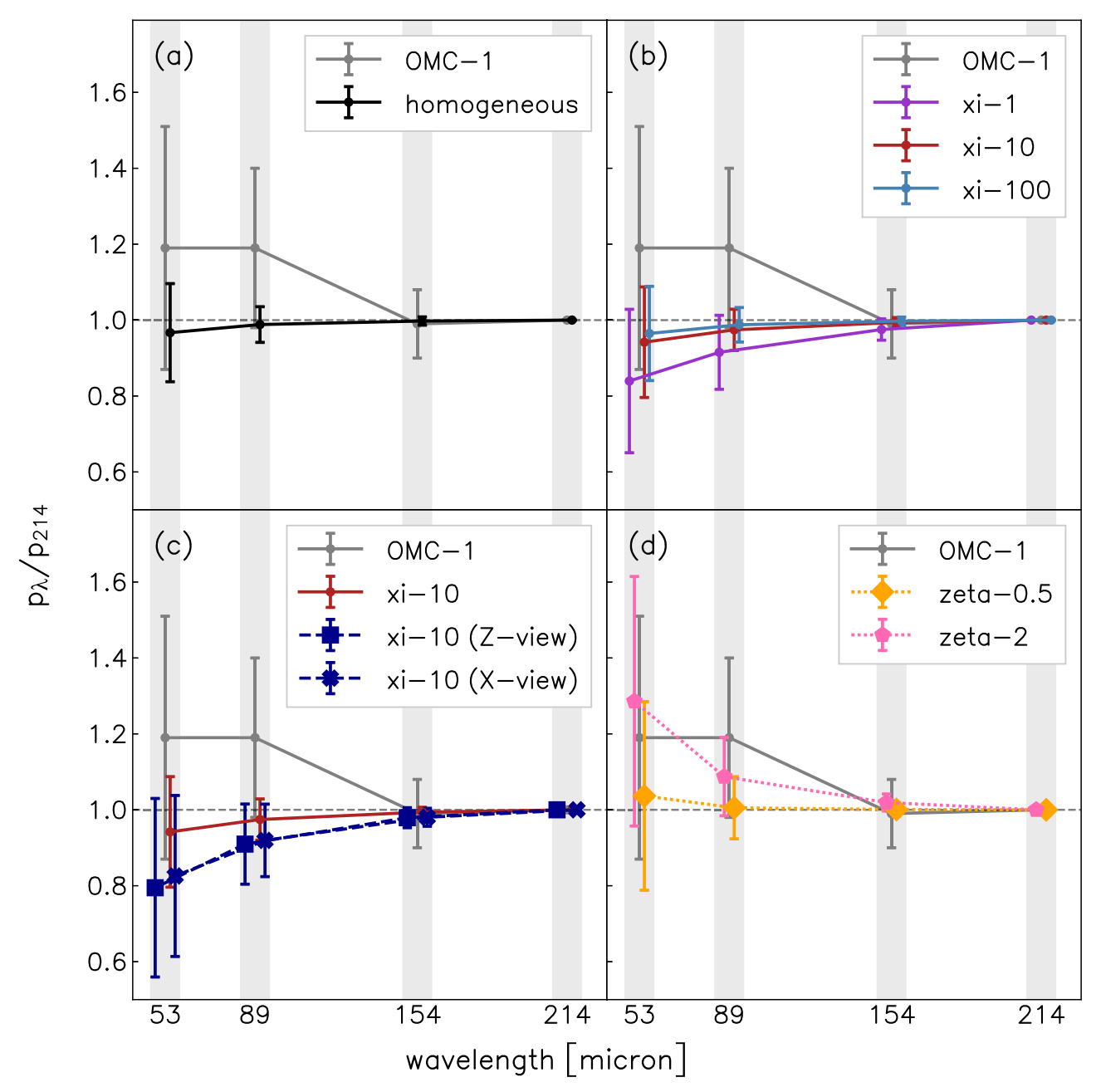


Figure 3. Global polarization spectrum for each set of synthetic observations (see Section 2.3). For better visibility, models are plotted with a slight offset at each HAWC+ band. The polarization spectrum computed for OMC-1 (Michail et al. 2021) is shown for comparison in gray. (a) Homogeneous grain alignment model (homogeneous). (b) Collisional depolarization grain alignment models varying the ξ parameter: 1, 10, and 100 (xi-1, xi-10, xi-100). (c) Our fiducial collisional depolarization grain alignment model (xi-10) for the nominal as well as two other viewing angles. (d) Temperature-dependent polarizability models where the polarizability is dependent on the temperature (zeta-0.5, zeta-2). The only model in this work that is able to produce a falling polarization spectrum comparable to OMC-1 is the zeta-2 temperature-dependent polarizability model shown in panel (d).

spectrum (i.e., polarization decreasing with wavelength). a_{ℓ} and b_{ℓ} are computed via a nonlinear least squares fit for each pixel. For each set of synthetic observations, the median and MAD values for the resulting linear fit parameters are listed in Table 2. We also include the results of the analogous analysis of OMC-1 in Michail et al. (2021).

Overall, these results show consistency with the results of the global polarization spectrum analysis in Section 3.1. Again, the homogeneous grain alignment model (homogeneous) as well as the collisional depolarization grain alignment model (xi-10) show flat or rising polarization spectra ($b_{\ell} \ge 0$). Negative values of b_{ℓ} are only seen for the temperature-dependent polarizability

Table 2
Median and MAD Values for the Resulting Pixel-by-pixel Linear
Parameter Fits

Model	a_{ℓ}	$b_{\ell} \times 1000 \; (\mu \text{m}^{-1})$
Homogeneous	1.00 ± 0.02	0.19 ± 0.72
xi-10	1.01 ± 0.02	0.36 ± 0.80
zeta-0.5	0.99 ± 0.03	-0.18 ± 1.39
zeta-2	0.96 ± 0.05	-1.65 ± 1.95
OMC-1 ^a	0.95 ± 0.05	-1.47 ± 2.04

Note.

^a OMC-1 results from Michail et al. (2021).

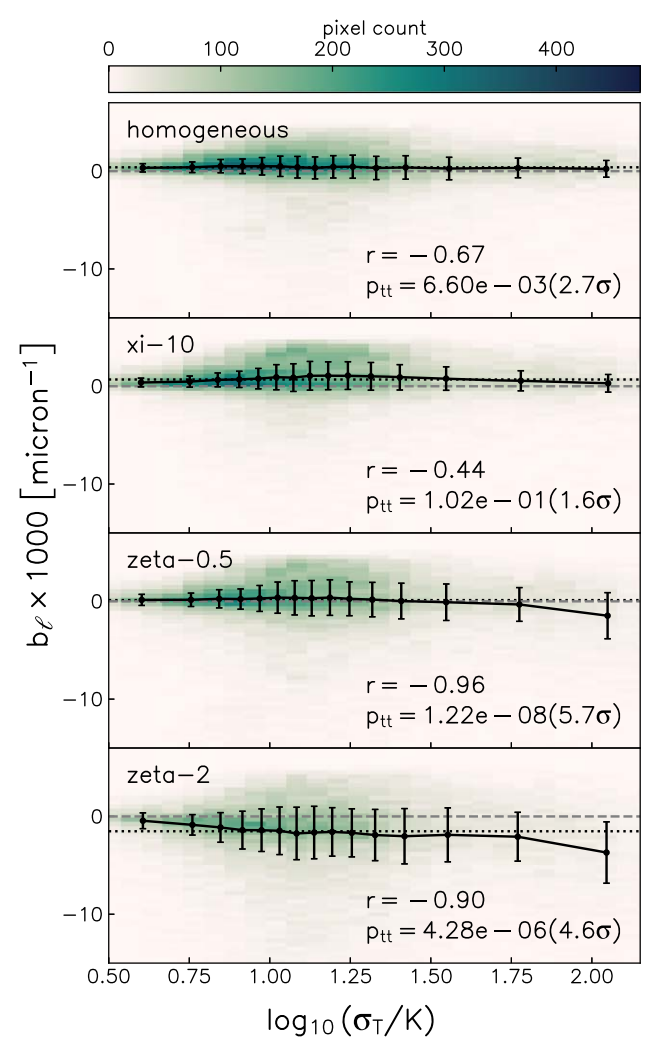


Figure 4. Correlation between the slope of the polarization spectrum (b_ℓ) and the standard deviation of the temperature along the line of sight (σ_T) for various grain alignment models. For each grain alignment model, each pixel is binned based on b_ℓ and σ_T . The black line plots the median b_ℓ at 15 equally sized bins in σ_T with the error bars indicating the MAD at that σ_T bin. The dashed gray line indicates $b_\ell = 0$ while the dotted black line shows the overall median b_ℓ of the grain alignment model. The two-tailed Pearson correlation coefficient (r) and associated two-tailed p-values (p_{tt}) are also shown. Only the temperature-dependent polarizability models show statistically significant correlations between σ_T and b_ℓ .

models with zeta-2 again showing the most steeply falling spectrum that matches OMC-1.

The HCE describes the scenario where a falling spectrum is achieved by the superposition of cooler, unaligned grains in dense regions along the line of sight with warmer, aligned grains in less dense regions. To assess whether the HCE is occurring in any of our models, we compare the slope of the polarization spectrum b_{ℓ} against the standard deviation of the voxel temperature along the line of sight (σ_T) in Figure 4. These voxel temperature values are derived from the original simulation data. We apply the two-tailed Pearson correlation coefficient test to compute the correlation coefficient (r) and associated two-tailed p-value (p_{tt}) on 15 equally sized binned median values. These are also shown in Figure 4. The only grain alignment models to exhibit any statistically significant correlation between b_{ℓ} and σ_T are the ones that include a temperature-dependent polarizability (i.e., zeta-0.5, zeta-2), which are also the only ones that show a falling spectrum. We discuss this further in Section 4.

3.2.1. Correlations of the Polarization Spectrum

Michail et al. (2021) explored the correlations between the polarization spectrum slope (i.e., b_{ℓ}) and the SED-fitting-derived temperature and column density maps obtained from Chuss et al. (2019). We apply this analysis to zeta-2—the model that best matches the falling spectrum result of OMC-1.

Figure 5 plots the slope of the polarization spectrum b_ℓ against the temperature and column density, respectively. The figure also shows the median and MAD slope values for 10 equally sized bins. In addition, using the two-tailed Pearson correlation coefficient test, we calculate the correlation coefficient (r) and associated two-tailed p-value (p_{tt}) on the equally sized binned median values. These statistics are shown in Figure 5. No robust correlation is found between b_ℓ and the temperature. However, we do find evidence of a statistically significant correlation between $N_{\rm H_2}$ and b_ℓ . We compute a Pearson correlation coefficient of r=0.90 with a significance of 3.5σ .

We note that the dust model used to compute temperature and column density for OMC-1 differs from the one used in our analysis. We use the dust model from Weingartner & Draine (2001), whereas the model used for the observations of OMC-1 assumes a modified blackbody fit incorporating a dust emissivity index (β) as a free parameter (Chuss et al. 2019). Replicating our analysis with the model from Chuss et al. (2019) does not alter any observed correlations (or lack thereof) between $N_{\rm H_2}$ and b_ℓ or between T and b_ℓ .

4. Discussion

4.1. Origin of the Falling Polarization Spectrum

While observations of the far-infrared spectrum in dense molecular clouds have typically attributed its shape to the HCE (Hildebrand et al. 1999; Vaillancourt et al. 2008; Zeng et al. 2013; Michail et al. 2021), there are a variety of different scenarios that could produce a falling far-infrared polarization spectrum.

In principle, it is possible for a falling spectrum to emerge without the consideration of any complexity in grain alignment or composition. For example, the falling spectrum (such as the one seen for OMC-1 in Figure 3) may arise purely as a consequence of magnetic field morphology. Cooler regions along the line of sight (traced well at longer wavelengths) tend to be denser and be undergoing the process of gravitational collapse and star formation. The magnetic field in these regions may therefore be more tangled and disordered, thus resulting in a lower polarization fraction (e.g., Chen et al. 2016). On the other hand, the magnetic field of warmer regions along the line of sight (traced well at shorter wavelengths), without these ongoing processes, is likely more ordered. As a result, even if we assume the grain alignment efficiency is the same, the observed polarization at longer wavelengths may suppressed.

In our model of homogeneous grain alignment, however, we find no evidence of a falling spectrum (see Figure 3(a)). As our simulations include variations in environmental conditions along the line of sight (as described in Section 2.2), this implies that temperature variations, field geometry, etc. along a sight line alone do not generally result in a falling spectrum. In other words, the inability of the uniform grain alignment model to reproduce the falling polarization spectrum implies that

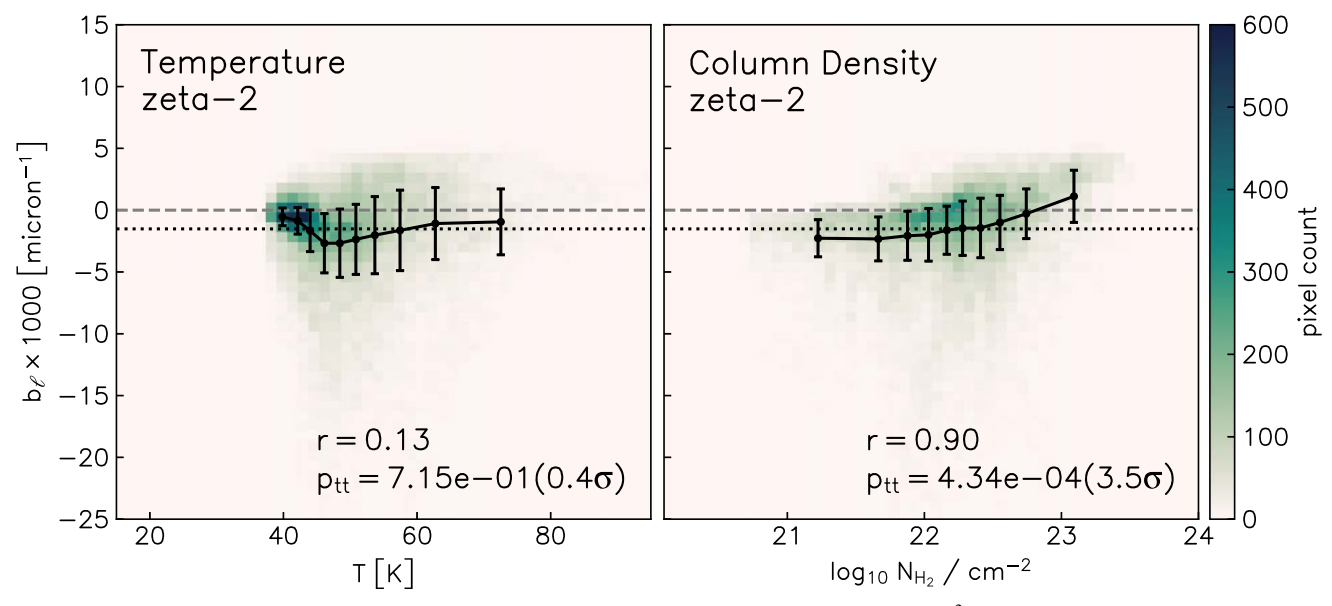


Figure 5. Correlations of b_ℓ with the temperature (left) and column density (right) for the zeta-2 model ($\alpha_p \propto T^2$). The black line indicates the median value of 10 equally sized bins. The error bars indicate the median absolute deviation value. The two-tailed Pearson correlation coefficient (r) and associated two-tailed p-values (p_{tt}) are also shown. The dashed gray line indicates $b_\ell = 0$ while the dotted black line indicates the overall median b_ℓ of the grain alignment model. zeta-2, the grain alignment model tested that most closely matches the polarization spectrum of OMC-1, indicates no significant correlation between b_ℓ and the temperature, but does show a significant correlation between b_ℓ and the column density. See Section 4.2 for more discussions.

variations in grain alignment efficiency are required to explain the falling spectrum.

The HCE posits that the falling spectrum originates from heterogeneous grain alignment efficiency: the line of sight includes both regions of cold unaligned grains and warmer regions of aligned grains. As cold regions can be cooler due to shielding from radiation, these colder regions are often denser. One possible source of heterogeneous grain alignment, for example, is the effect of local density. High-density regions facilitate more gas–grain collisions that serve to "unalign" grains (Andersson et al. 2015). However, depolarization can also result from elevated temperatures disrupting grain alignment in regions of more modest densities.

To evaluate the possibility of such potentially competing effects, we consider the results from the grain alignment prescription from Lam et al. (2021) as described in Section 2.3. By varying the value of the alignment parameter ξ (i.e., $\times i-1$, $\times i-100$), we are able to explore the dependence of polarization on collisional dealignment. Nonetheless, the falling spectrum expected of HCE is not observed (see Figures 3(b) and (c)).

As shown in Figure 4, we find evidence that the grain collisions are incapable of producing the HCE. Like the homogeneous grain model, it shows no correlation between σ_T —a proxy for temperature heterogeneity along a line of sight—and the slope of the polarization spectrum. For these collisional depolarization grain alignment models, there is no evidence that the superposition of different temperatures along the line of sight is causing a falling spectrum. As such, we find that a collisional depolarization grain model is unable to produce a falling spectrum.

In Section 2.3, we constructed two models to emulate HCE by incorporating a relation between the emitted polarized emission at each voxel and the local temperature: zeta-0.5 and zeta-2. As shown in Figure 3(d), these two models represent the only models that are able to produce a falling spectrum. While both models produced a falling spectrum, it is

the model that has a stronger dependence on the temperature that delivers a polarization spectrum comparable to that observed in OMC-1: $\alpha_p \propto T^2$ (zeta-2).

Considering all the grain alignment models discussed in this work, the evidence implies that variations in the grain alignment efficiency are required for a falling polarization spectrum (i.e., a homogeneous grain alignment model is insufficient). Additionally, we find that models that include collisional dealignment fail to produce a falling spectrum. However, we do not rule out the possibility of other density-related effects. For example, it is possible that grain growth or coagulation may also influence the shape of the polarization spectrum (Ysard et al. 2013). Nonetheless, we find that only our grain alignment model that is coupled to the temperature is able to reproduce the falling far-infrared polarization spectrum. This suggests that a falling spectrum and the HCE can be explained by RATs or similar mechanisms where grain alignment is enhanced by ambient radiation sources.

Simulations from Bethell et al. (2007) do not produce a falling polarization spectrum despite including a realistic molecular cloud as well as a prescription for RATs. In comparing their polarization spectrum results with those from observations, Bethell et al. (2007) note that their simulations only include the interstellar radiation field and suggest that the existence of the falling spectrum is due to the presence of embedded sources—something not included in their simulation. The simulation used in our work does include embedded sources (the forming protostars; see Section 2.2) suggesting that the presence of embedded radiation sources may indeed be essential for the falling polarization spectrum to be produced.

4.2. Polarization Spectrum Correlations

While we find a polarization spectrum comparable to that observed in OMC-1 when we use a simulation where the fractional polarization depends on the temperature (i.e., zeta-2), we do not find the same correlations that Michail et al. (2021) find

between the slope of the polarization spectrum and the temperature. In particular, for OMC-1, Michail et al. (2021) find a robust positive correlation between b_ℓ and T ($r\!=\!0.93$, $p_{\rm tt}\!=\!6.5\times10^4$, 3.4σ). We find no such correlation in our results between b_ℓ and T. On the other hand, while Michail et al. (2021) find no correlation between the slope of the polarization spectrum and the column density, our simulations show a statistically significant positive correlation between b_ℓ and $N_{\rm H_2}$ (i.e., regions of lower column density show a more steeply falling spectrum).

Taken together, Michail et al. (2021) present their correlations in OMC-1 as evidence for RATs as the explanation for HCE. The authors argue that it is the lack of radiation (as traced by lower dust temperature) that causes loss of alignment and not any intrinsic high column density effect. We can then ask why—despite exhibiting the HCE—do we not find similar correlations in our zeta-2 ($\alpha_p \propto T^2$) model?

4.2.1. Correlations between N_{H_2} and b_{ℓ}

A possible origin for the positive correlation between the column density and b_{ℓ} is wavelength-dependent polarization by absorption due to differences in optical depth at different wavelengths. The polarized emission from deep in the cloud can be absorbed by the aligned grains closer to the surface. While this effect is generally negligible for clouds that are optically thin, it can be more pronounced at sufficiently high optical depths. As the optical depth increases at shorter wavelengths, this will have the result of lowering the observed polarization at the shorter wavelengths, effectively increasing the value of b_{ℓ} and thereby producing a more positive slope.

To test this, we model the effect that optical-depth-induced absorption may have on the slope of the polarization. We follow the formalism from Novak et al. (1989) that calculates the magnitude of the optical-depth-induced reduction in the degree of polarization assuming a uniform magnetic field direction. Here, $p_{m,\lambda}$ is the measured polarization fraction at wavelength λ while $p_{0,\lambda}$ represents the polarization fraction if there were no absorption. The emissivity at a given wavelength, ε_{λ} , is given by $\varepsilon_{\lambda} = 1 - \exp(-\tau_{\lambda})$ for arbitrary optical depth (τ_{λ}) . To first order, we can approximate this effect as

$$\frac{p_{m,\lambda}}{p_{0,\lambda}} = -\frac{1}{\varepsilon_{\lambda}} (1 - \varepsilon_{\lambda}) \ln(1 - \varepsilon_{\lambda}). \tag{12}$$

From our simulations for the four wavelength bands, we integrated along each sight line to obtain the optical depth using the dust model from Weingartner & Draine (2001). These optical depth values are then used to compute ε_{λ} . Assuming an initially flat polarization spectrum (i.e., $p_{0,53} = p_{0,89} = p_{0,154} = p_{0,214}$), we follow Equation (12) to estimate $p_{m,\lambda}$ and produce a model polarization spectrum.

To investigate how this model polarization spectrum correlates with the column density, we compute b_{ℓ} and compare it to the column density. This model is shown in Figure 6 in orange. Like our simulation result, this model shows a positive correlation between b_{ℓ} and the column density. While the orange curve is based on assuming an intrinsically flat spectrum, assuming an intrinsically falling or rising spectrum yields a similarly shaped curve. We emphasize the that model from Novak et al. (1989), unlike our simulations, assumes a uniform magnetic field direction. As such, this comparison is only approximate. Nonetheless, we

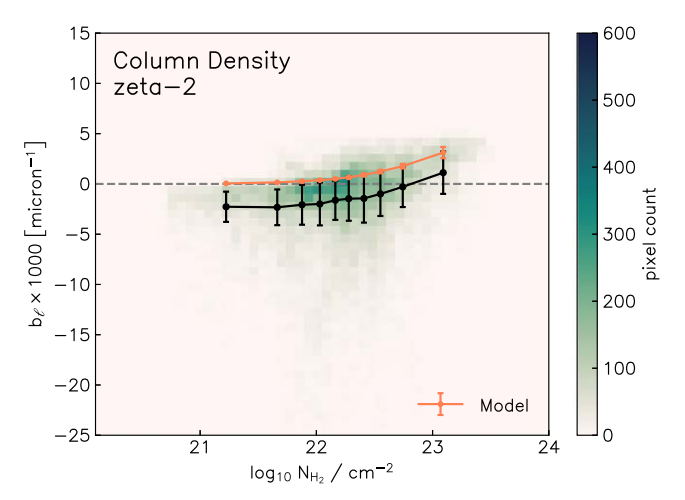


Figure 6. Correlation between b_ℓ and the column density for the model zeta-2 (shown in black) as in the right panel of Figure 5, overplotted with the optical depth model (shown in orange) adopted from Novak et al. (1989; see Section 4.2.1). The dashed gray line indicates $b_\ell = 0$. The two $b_\ell - N_{\rm H_2}$ curves are similar indicating that the $b_\ell - N_{\rm H_2}$ correlation measured in our synthetic observation may be due to an optical depth effect.

suggest that the correlations between b_{ℓ} and $N_{\rm H_2}$ can at least partially be attributed to this optical depth effect.

Furthermore, we note that there is a slight rise in the value of b_{ℓ} for the highest column density bin of OMC-1 (See Figure 4 in Michail et al. 2021). As such, we conclude that optical depth effects can influence the observed far-infrared polarization spectra of star-forming clouds, and alter correlations of the spectrum properties with the column density.

4.2.2. Correlations between T and be

While our temperature-dependent polarizability grain alignment models show features of the HCE, they do not show a positive correlation between b_ℓ and T (see Figure 5). We do note that our simulated cloud is warmer when compared to OMC-1 (see Figure 2) and that this is likely the result of the 35 K initial simulation temperature and temperature floor imposed by the simulation (detailed in Section 2.2). As such it is possible that the temperature floor is artificially affecting potential correlations. For example, a positive correlation may otherwise be visible should the simulation have had an initial gas temperature of less than 35 K. While we cannot completely rule out all potential effects of this temperature difference on the correlations between T and b_ℓ , we note that only a small fraction of the simulation voxels are likely reset by this artificial temperature floor.

Regardless, we suggest there is no reason to necessarily expect a relation between these two parameters for a cloud with the HCE. As described in Hildebrand et al. (1999), the crucial element of the HCE is the presence of both warmer and cooler components along the same sight line. The "average" or any single temperature determined for the sight line—such as that calculated from a SED fit—does not describe the presence of warmer and cooler components. By contrast, using σ_T as described in Section 3.2, we can directly investigate the superposition of warmer and cooler components. As shown in Figure 4, we find that our zeta-2 model shows a clear correlation between b_ℓ and the σ_T . This provides evidence that a correlation between b_ℓ and T is not required for simulations that exhibit HCE.

5. Conclusions

We generate synthetic far-infrared polarization spectra using a fully 3D, RMHD star-forming simulation and compare it with SOFIA/HAWC+ observations of OMC-1 (Michail et al. 2021). By varying the grain alignment prescriptions used to generate the synthetic observations from our simulations, we investigated the origin of the far-infrared falling spectrum seen in observations of star-forming molecular clouds.

Our principal conclusions are as follows:

- 1. We were not able to obtain a far-infrared falling polarization spectrum (negative slope of p versus, λ) comparable to that observed in OMC-1 using a homogeneous grain alignment model. The polarization spectrum of our simulation using a homogeneous grain alignment model is flat.
- 2. Similarly, with the inclusion of collisional depolarization through the grain alignment model of Lam et al. (2021), the polarization spectrum continues to be flat or rising. This remains the case along various viewing angles and for various values of the model parameter ξ that is controlled by e.g., grain size and grain magnetic susceptibility. While collisional depolarization cannot produce a falling polarization spectrum, we note that other effects such as grain growth and coagulation (Ysard et al. 2013) may also play a role and thus warrant further investigation.
- 3. Extending this collisional depolarization grain alignment model by including temperature-dependent polarizability does result in a falling polarization spectrum. While these temperature-dependent polarizability models are not based on a realistic treatment of RATs and only represent a simple emulation of the expected feature of RATs, we find that both the zeta-0.5 and zeta-2 models are capable of producing a falling polarization spectrum. The polarization spectrum of the zeta-2 model, where $\alpha_p \propto T^2$, is most consistent with the OMC-1 observations. Furthermore, among the models evaluated here, the temperaturedependent polarizability models are the only ones that provide evidence for the HCE. Thus, HCE caused by RATs is a plausible explanation for the falling polarization spectrum. However, we note that the temperature-dependent polarizability models used in this work represent a simple emulation of the features of RATs. As such, future work using more sophisticated models of grain alignment (such as POLARIS; Reissl et al. 2016) should be used to verify this relation.
- 4. For the model that most closely matches OMC-1 (zeta-2), we find a positive correlation between the column density and the slope of the polarization spectrum. We find that this can be the result of optical-depth-induced depolarization, suggesting that optical depth effects can affect the observed far-infrared polarization spectra and potentially alter correlations of the spectrum properties with the column density.
- 5. In contrast to Michail et al. (2021), despite finding a similar overall falling spectrum in zeta-2, we find no evidence of a correlation between the temperature and the polarization spectrum slope. We suggest that this feature need not exist for HCE to explain the overall falling spectrum and may not be an expected general consequence from HCE.

In summary, our investigation of a series of grain alignment models in a realistic, fully 3D RMHD star-forming molecular cloud—comparable to OMC-1—suggests that a falling polarization spectrum requires variations in the grain alignment efficiency. While we find evidence that HCE caused by RATs can explain the falling polarization spectrum, we suggest that further investigations with more sophisticated grain alignment models are required.

Acknowledgments

We thank the anonymous referee for the helpful comments. This work is based on observations made with the NASA/DLR Stratospheric Observatory for Infrared Astronomy (SOFIA). SOFIA is jointly operated by the Universities Space Research Association, Inc. (USRA), under NASA contract NNA17BF53C, and the Deutsches SOFIA Institut (DSI) under DLR contract 50 OK 2002 to the University of Stuttgart. Financial support for this work was provided by NASA through award #09-0535 to Villanova University issued by USRA. The numerical simulation considered in this study was supported by NASA through a NASA ATP grant NNX17AK39G as well as the NASA High-End Computing (HEC) Program through the NASA Advanced Supercomputing (NAS) Division at Ames Research Center, and by the National Energy Research Scientific Computing Center (NERSC), a U.S. Department of Energy Office of Science User Facility located at Lawrence Berkeley National Laboratory, operated under Contract No. DE-AC02-05CH11231 using NERSC award NP-ERCAP0023065. This work used computing resources provided by Northwestern University and the Center for Interdisciplinary Exploration and Research in Astrophysics (CIERA). This research was supported in part by the computational resources and staff contributions provided for the Quest high-performance computing facility at Northwestern University, which is jointly supported by the Office of the Provost, the Office for Research, and Northwestern University Information Technology. This work was performed under the auspices of the U.S. Department of Energy (DOE) by Lawrence Livermore National Laboratory under Contract DE-AC52-07NA27344 (C.Y.C.). LLNL-JRNL-862957. E.G.C. acknowledges support from the National Science Foundation MPS-Ascend Postdoctoral Research Fellowship under grant No. 2213275. Z.Y.L. is supported in part by NSF AST-2307199 and NASA 80NSSC20K0533.

Facility: SOFIA (HAWC+).

Software: python, numpy (Harris et al. 2020), matplotlib (Hunter 2007), scipy (Virtanen et al. 2020), astropy (Astropy Collaboration et al. 2013, 2018, 2022), aplpy.

ORCID iDs

Dennis Lee https://orcid.org/0000-0002-3455-1826 Che-Yu Chen https://orcid.org/0000-0002-9209-7916 Giles Novak https://orcid.org/0000-0003-1288-2656 David T. Chuss https://orcid.org/0000-0003-0016-0533 Erin G. Cox https://orcid.org/0000-0002-5216-8062 Kaitlyn Karpovich https://orcid.org/0009-0006-4830-163X Zhi-Yun Li https://orcid.org/0000-0002-7402-6487 Joseph M. Michail https://orcid.org/0000-0003-3503-3446

References

Andersson, B. G., Lazarian, A., & Vaillancourt, J. E. 2015, ARA&A, 53, 501 Ashton, P. C., Ade, P. A. R., Angilè, F. E., et al. 2018, ApJ, 857, 10

```
Astropy Collaboration, Price-Whelan, A. M., Lim, P. L., et al. 2022, ApJ,
  935, 167
Astropy Collaboration, Price-Whelan, A. M., Sipőcz, B. M., et al. 2018, AJ,
  156, 123
Astropy Collaboration, Robitaille, T. P., Tollerud, E. J., et al. 2013, A&A,
   558, A33
Bethell, T. J., Chepurnov, A., Lazarian, A., & Kim, J. 2007, ApJ, 663, 1055
Chandrasekhar, S., & Fermi, E. 1953, ApJ, 118, 113
Chen, C.-Y., King, P. K., & Li, Z.-Y. 2016, ApJ, 829, 84
Chen, C.-Y., King, P. K., Li, Z.-Y., Fissel, L. M., & Mazzei, R. R. 2019,
          S, 485, 3499
Chen, C.-Y., Li, Z.-Y., Mazzei, R. R., et al. 2022, MNRAS, 514, 1575
Chuss, D. T., Andersson, B. G., Bally, J., et al. 2019, ApJ, 872, 187
Crutcher, R. M. 2012, ARA&A, 50, 29
Cunningham, A. J., Klein, R. I., Krumholz, M. R., & McKee, C. F. 2011, ApJ,
   740, 107
Davis, L. 1951, PhRv, 81, 890
Dolginov, A. Z., & Mitrofanov, I. G. 1976, Ap&SS, 43, 291
Draine, B. T., & Weingartner, J. C. 1997, ApJ, 480, 633
Fiege, J. D., & Pudritz, R. E. 2000, ApJ, 544, 830
Gandilo, N. N., Ade, P. A. R., Angilè, F. E., et al. 2016, ApJ, 824, 84
Harper, D. A., Runyan, M. C., Dowell, C. D., et al. 2018, JAI, 7, 1840008
Harris, C. R., Millman, K. J., van der Walt, S. J., et al. 2020, Natur, 585, 357
Hildebrand, R. H., Davidson, J. A., Dotson, J. L., et al. 2000, PASP, 112, 1215
Hildebrand, R. H., Dotson, J. L., Dowell, C. D., Schleuning, D. A., &
   Vaillancourt, J. E. 1999, ApJ, 516, 834
Hildebrand, R. H., Kirby, L., Dotson, J. L., Houde, M., & Vaillancourt, J. E.
   2009, ApJ, 696, 567
Houde, M., Hull, C. L. H., Plambeck, R. L., Vaillancourt, J. E., &
  Hildebrand, R. H. 2016, ApJ, 820, 38
```

Houde, M., Vaillancourt, J. E., Hildebrand, R. H., Chitsazzadeh, S., &

Kounkel, M., Hartmann, L., Loinard, L., et al. 2017, ApJ, 834, 142

Lam, K. H., Chen, C.-Y., Li, Z.-Y., et al. 2021, MNRAS, 507, 608

Kirby, L. 2009, ApJ, 706, 1504

Hunter, J. D. 2007, CSE, 9, 90

```
Lazarian, A., & Hoang, T. 2007, MNRAS, 378, 910
Lee, D., Berthoud, M., Chen, C.-Y., et al. 2021, ApJ, 918, 39
Li, A., & Draine, B. T. 2001, ApJ, 554, 778
Li, H. B., Goodman, A., Sridharan, T. K., et al. 2014, in Protostars and Planets
   VI, ed. H. Beuther et al. (Tuscon, AZ: Univ. Arizona Press), 101
Li, P., Cunningham, A., Gaches, B., et al. 2021, JOSS, 6, 3771
Li, P. S., Lopez-Rodriguez, E., Ajeddig, H., et al. 2022, MNRAS, 510, 6085
Li, P. S., Martin, D. F., Klein, R. I., & McKee, C. F. 2012, ApJ, 745, 139
Li, P. S., McKee, C. F., & Klein, R. I. 2015, MNRAS, 452, 2500
Michail, J. M., Ashton, P. C., Berthoud, M. G., et al. 2021, ApJ, 907, 46
Motte, F., Bontemps, S., & Louvet, F. 2018, ARA&A, 56, 41
Novak, G., Gonatas, D. P., Hildebrand, R. H., Platt, S. R., & Dragovan, M.
   1989, ApJ, 345, 802
Offner, S. S. R., Klein, R. I., McKee, C. F., & Krumholz, M. R. 2009, ApJ,
   703, 131
Ostriker, E. C., Stone, J. M., & Gammie, C. F. 2001, ApJ, 546, 980
Pattle, K., & Fissel, L. 2019, FrASS, 6, 15
Pattle, K., Fissel, L., Tahani, M., Liu, T., & Ntormousi, E. 2023, in ASP Conf.
   Ser. 534, Protostars and Planets VII, ed. S. Inutsuka et al. (San Francisco,
   CA: ASP), 193
Planck Collaboration, Ade, P. A. R., Aghanim, N., et al. 2016, A&A,
   586, A138
Reissl, S., Wolf, S., & Brauer, R. 2016, A&A, 593, A87
Semenov, D., Henning, T., Helling, C., Ilgner, M., & Sedlmayr, E. 2003, A&A,
  410, 611
Shariff, J. A., Ade, P. A. R., Angilè, F. E., et al. 2019, ApJ, 872, 197
Soler, J. D. 2019, A&A, 629, A96
Soler, J. D., Hennebelle, P., Martin, P. G., et al. 2013, ApJ, 774, 128
Vaillancourt, J. E., Dowell, C. D., Hildebrand, R. H., et al. 2008, ApJL,
  679. L25
Virtanen, P., Gommers, R., Oliphant, T. E., et al. 2020, NatMe, 17, 261
Weingartner, J. C., & Draine, B. T. 2001, ApJ, 548, 296
Yang, H. 2021, ApJ, 911, 125
Ysard, N., Abergel, A., Ristorcelli, I., et al. 2013, A&A, 559, A133
Zeng, L., Bennett, C. L., Chapman, N. L., et al. 2013, ApJ, 773, 29
```